

A Bayesian Analysis of Nuclear Deformation Properties with Skyrme Energy Functionals

N. Schunck¹, K. R. Quinlan², J. Bernstein²

¹ Nuclear and Chemical Sciences Division, Lawrence Livermore National Laboratory, Livermore, CA 94551, USA

² Applied Statistics Group, Lawrence Livermore National Laboratory, Livermore, CA 94551, USA

E-mail: schunck1@llnl.gov

May 2020

Abstract. In spite of numerous scientific and practical applications, there is still no comprehensive theoretical description of the nuclear fission process based solely on protons, neutrons and their interactions. The most advanced simulations of fission are currently carried out within nuclear density functional theory (DFT). In spite of being fully quantum-mechanical and rooted in the theory of nuclear forces, DFT still depends on a dozen or so parameters characterizing the energy functional. Calibrating these parameters on experimental data results in uncertainties that must be quantified for applications. This task is very challenging because of the high computational cost of DFT calculations for fission. In this paper, we use Gaussian processes to build emulators of DFT models in order to quantify and propagate statistical uncertainties of theoretical predictions for a range of nuclear deformations relevant to describing the fission process.

PACS numbers: 21.10.-k, 21.30.Fe, 21.60.Jz, 21.65.Mn

Submitted to: *J. Phys. G: Nucl. Phys.*

1. Introduction

Nuclear fission plays a key role in a number of basic and applied science problems, from understanding the origin of elements in the universe [1] to the stability of superheavy elements [2]. From a fundamental science perspective, one would like to be able to describe nuclear fission in a fully quantum-mechanical way as emerging from nuclear forces within the nucleus. Such a “microscopic” picture poses formidable challenges to theorists as it would require solving the quantum many-body problem of fermions in interaction even though nuclear forces remain poorly known. Currently, nuclear density functional theory represents our best attempt to tackle such a problem [3].

Density functional theory (DFT) is a general approach to the quantum many-body problem that is designed to scale well with particle number [4, 5]. In the particular case of nuclear physics, effective, in-medium nuclear forces are encoded in an energy density functional (EDF), which is a function of the intrinsic density of nucleons. Given this EDF, various theoretical techniques allow computing a number of nuclear properties ranging from ground-state properties, low-lying excited spectra or large-amplitude collective motion such as fission or nuclear reactions [6].

While DFT has been successfully applied in many areas of nuclear science, it should be viewed as an imperfect, phenomenological model. In particular, the parameters of the EDF are unknown and must be calibrated on a set of experimental data, and this process depends on the particular level of approximation within DFT [7, 8, 9]. Over the past decade, there have been numerous attempts to quantify the uncertainties of this calibration on predictions, but these earlier studies have focused mostly on various ground-state properties such as masses [10, 11, 12, 13], drip-line properties [14, 15], or neutron skin [16, 17]. There are still relatively few examples where either covariance or Bayesian techniques were applied to more complex problems such as collective excitations [18] or fission barriers [19]. Yet, in light of the computational cost of fission calculations, such analyses are essential to better identify model weaknesses.

The main goal of this paper is to assess whether standard statistical methods such as Bayesian inference with Gaussian processes can be used with confidence in the emulation and uncertainty quantification of fission models. Specifically, we wish to extend the work of [19] to (i) build an emulator of fission pathways and (ii) build an emulator of the location and characteristics of scission configurations (the point where the two fragment are formed) and (iii) determine the posterior distribution of EDF parameters conditioned on fission barriers .

Our paper is organized in three main sections. Section 2 recalls some basic elements of nuclear energy density functional theory for the particular case of Skyrme functionals. In section 3, we summarize the statistical models that we used in the analysis including Gaussian processes and Bayesian inference with Markov-Chain Monte-Carlo sampling. Finally, we show in section 4 a selection of results for the benchmark case of the potential energy curve of the ^{240}Pu nucleus.

2. Physics Background

In this section, we give a brief summary of the (single-reference) energy density functional theory with Skyrme generators that will be used throughout this paper.

2.1. Nuclear Energy Density Functional Theory

The general framework for this work is the Hartree-Fock-Bogoliubov (HFB) theory, where the nuclear many-body wave function takes the form of a quasiparticle vacuum [6, 20, 21]. In the HFB approximation, all degrees of freedom for the system are encoded in the one-

body density matrix ρ and pairing tensor κ (and its complex conjugate κ^*). In particular, the total energy of the nucleus reads

$$E[\rho, \kappa, \kappa^*] = E_{\text{nuc}}[\rho] + E_{\text{Cou}}[\rho] + E_{\text{pair}}[\rho, \kappa, \kappa^*]. \quad (1)$$

Here, we use a Skyrme-like energy density functional (EDF) for the nuclear part,

$$E_{\text{nuc}}[\rho] = \sum_{t=0,1} \int d^3\mathbf{r} \chi_t(\mathbf{r}), \quad (2)$$

where the Skyrme EDF includes the kinetic energy term and reads

$$\chi_t(\mathbf{r}) = C_t^{\rho\rho} \rho_t^2 + C_t^{\rho\tau} \rho_t \tau_t + C_t^{JJ} \mathbf{J}_t^2 + C_t^{\rho\Delta\rho} \rho_t \Delta\rho_t + C_t^{\rho\nabla J} \rho_t \nabla \cdot \mathbf{J}_t. \quad (3)$$

In this expression, the index t refers to the isoscalar ($t = 0$) or isovector ($t = 1$) channel. We refer to Refs. [22, 23, 24, 25, 26] for the definition of the densities ρ , τ , \mathbf{J} , and \mathbf{J} . There are 8 real-valued coupling constants $C_t^{uu'}$ for $t = 0, 1$ and $uu' = (\rho\tau, JJ, \rho\Delta\rho, \rho\nabla J)$. The case of $C_t^{\rho\rho}$ is a little different, since it is a function of the density $\rho(\mathbf{r})$,

$$C_t^{\rho\rho} = C_{t0}^{\rho\rho} + C_{tD}^{\rho\rho} \rho_0^\gamma(\mathbf{r}). \quad (4)$$

This density-dependent term is thus characterized by 5 parameters, the two $C_{t0}^{\rho\rho}$ and $C_{tD}^{\rho\rho}$ and the exponent γ . Therefore, $E_{\text{nuc}}[\rho]$ is fully characterized by 13 parameters.

The Coulomb term in (1) is computed at the Hartree-Fock approximation with the exchange term treated at the Slater approximation [24]. The pairing energy is computed from a surface-volume density-dependent pairing force

$$V_q(\mathbf{r}, \mathbf{r}') = V_0^q \left[1 - \frac{1}{2} \frac{\rho(\mathbf{r})}{\rho_c} \right] \delta(\mathbf{r} - \mathbf{r}'), \quad (5)$$

where q here refers to the type of particle (proton or neutron) and $\rho_c = 0.16 \text{ fm}^{-3}$. Including the pairing channel in the fit thus adds 2 more parameters to the fit. As customary for zero-range pairing forces, a cut-off at $E_{\text{cut}} = 60 \text{ MeV}$ is introduced to limit the number of quasiparticles used when calculating the density matrix.

In the context of fission, potential energy curves (or surfaces) are obtained by adding constraints on the density ρ . The constraints are typically the expectation value of suitable operators on the HFB vacuum. In this work, we will consider only one constraint on the expectation value of the axial quadrupole moment $q \equiv \langle \hat{Q}_{20} \rangle$. The total HFB energy at the deformation q is thus the scalar function $E(q)$. It implicitly depends on the vector of coupling constants $\mathbf{x} \equiv \{C_t^{uu'}\}$ of the energy density functional, $E \equiv E(q; \mathbf{x})$.

2.2. Parameters and Numerical Implementation

Following [27], we express the coupling constants $C_{t0}^{\rho\rho}$, $C_{tD}^{\rho\rho}$, γ and $C_t^{\rho\tau}$ as a function of the parameters of infinite nuclear matter. Our analysis will be focused on the UNEDF1_{HFB} functional, for which the two tensor coupling constants are 0 and the vector effective mass is set at the SLy4 value, $m_v^* = 1.249838$ [28]. As a result, the actual vector \mathbf{x} of parameters is

$$\mathbf{x} = \left(E^{\text{NM}}, \rho_{\text{sat}}, K^{\text{NM}}, a_{\text{sym}}^{\text{NM}}, L_{\text{sym}}^{\text{NM}}, m_s^*, C_0^{\rho\Delta\rho}, C_1^{\rho\Delta\rho}, C_0^{\rho\nabla J}, C_1^{\rho\nabla J}, V_0^n, V_0^p \right) \quad (6)$$

and the total number of parameters under consideration is $n = 12$.

Calculations were performed with the latest version of the code HFODD [29]. The solutions to the HFB equation are expanded on a deformed basis of $N_{\text{shell}} = 30$ shells. For each value of the quadrupole moment, the oscillator length and axial quadrupole deformation of the basis, which determines the ratios of oscillator frequencies ω_z/ω_x , are set according to the empirical formula of [30]. The Gauss-Hermite integration mesh comprises 40 points in the x - and y -directions and 66 in the z -direction. We use linear constraints on the quadrupole moment (and on the dipole moment to fix the position of the center of mass), and the value of the Lagrange parameter is set at each iteration based on the cranking approximation of the QRPA matrix.

3. Statistical methods

In this section we first introduce our Gaussian Process emulator of the potential energy curves $E(q; \mathbf{x})$ and then describe how this emulator will be used to generate a posterior distribution of the parameters.

3.1. Gaussian Process Emulator

To emulate the potential energy curves, we use a Gaussian Stochastic Process (GaSP) emulator as described in [31]. To implement a GaSP, the data should be observed at the same input locations for all curves, i.e., all potential energy curves must be defined on the same grid of deformations q . A GaSP $y(\cdot)$ can be defined as

$$y(\cdot) \sim \text{GaSP}(\mu(\cdot), \sigma^2 C(\cdot, \cdot)), \quad (7)$$

with μ the mean function, σ^2 the variance and C the correlation function. Here the mean function is modeled as a linear combination of basis functions $\mathbf{h}(\mathbf{x}) \equiv (h_1(\mathbf{x}), \dots, h_q(\mathbf{x}))$ and regression parameters $\boldsymbol{\kappa} \equiv (\kappa_1, \dots, \kappa_q)$ so that

$$\mu(\mathbf{x}) = E[y(\mathbf{x})] = \mathbf{h}(\mathbf{x}) \cdot \boldsymbol{\kappa} = \sum_{t=1}^q h_t(\mathbf{x}) \kappa_t. \quad (8)$$

The correlation function is defined by the Matérn covariance structure. We apply a common specific case referred to as the Matérn 5/2,

$$C(\mathbf{x}, \mathbf{x}') = \left(1 + \frac{\sqrt{5} \|\mathbf{x} - \mathbf{x}'\|}{\gamma} + \frac{5\|\mathbf{x} - \mathbf{x}'\|^2}{3\gamma^2} \right) \exp\left(-\frac{\sqrt{5}\|\mathbf{x} - \mathbf{x}'\|}{\gamma} \right), \quad (9)$$

where γ is a hyper-parameter that is optimized to obtain a better fit. This correlation structure is stationary, meaning that the correlation is assumed to only depend on the distance between two observations, i.e., $\|\mathbf{x} - \mathbf{x}'\|$, but not based on the location of those observations. Note that each deformation q is treated independently of the others. This model is fit using the RobustGaSP R package [32]. The default setting uses a constant mean for $\mu(\mathbf{x})$ but first subtracts the mean at each input location. The model is robust in terms of the estimation of hyperparameters such as γ . It avoids numerical issues while still achieving good predictive performance.

3.2. Bayesian Regression

We now discuss the Bayesian framework that will be used to find posterior distributions of the parameters. The philosophy of Bayesian inference starts with the fact that there is a prior probability distribution representing the *a priori* beliefs or knowledge about the parameter set. This prior state of knowledge is updated when presented with the observed experimental data to give a posterior probability distribution representing the current state of knowledge given the data. Formally, our goal is to determine the posterior distribution of the parameters \mathbf{x} represented as $\pi(\mathbf{x}|y)$ using observations y_1, \dots, y_n using the formula

$$\pi(\mathbf{x}|y) \propto L_y(\mathbf{x})\pi(\mathbf{x}), \quad (10)$$

where $\pi(\mathbf{x})$ is the prior distribution and L is the likelihood function of the data (the theoretical prediction of the model) given the parameters. Here we use a normal likelihood function justified by assuming Gaussian measurement errors. Given a set $\{d_i\}_{i=1, n_d}$ of n_d experimental values (in our case the three measurements in Table 2) for some observables and $\{y_i(\mathbf{x})\}_{i=1, n_d}$ the theoretical predictions obtained from the GaSP emulator at \mathbf{x} for these same observables, then the likelihood function reads

$$L_y(\mathbf{x}) \propto \left(\prod_{i=1}^{n_d} \sigma_i^2 \right)^{\frac{n_d}{2}} \exp \left(- \sum_{i=1}^{n_d} \frac{(y_i(\mathbf{x}) - d_i)^2}{2\sigma_i^2} \right), \quad (11)$$

where σ_i^2 is the variance for each experimental value. The advantage of Bayesian inference is that our result is a full distribution which allows us to make statements about the uncertainty of our parameter estimates. The difficulty here is that an analytic form of the posterior distribution can only be found under specific distributional assumptions on the prior and likelihood function. These assumptions are not always realistic, and as such approximations of the posterior are typically made using Markov Chain Monte Carlo (MCMC) sampling techniques. These methods yield a large number of approximately independent samples from a Markov chain that should have the same distribution as the posterior. Here, we select non-informative prior distributions that are uniform over the given parameter boundaries. This implies that we have no prior knowledge of which region of the parameter space is closer to the “real value”; we only assume that it will occur somewhere in the specified region.

We apply a Delayed Rejection Adaptive Metropolis MCMC algorithm [33]. The Delayed Rejection algorithm samples a second value when a proposed value is rejected. This second proposal is typically drawn from a proposal distribution with a smaller variance. We use a maximum number of delayed rejections of one at each iteration. It is possible to do this multiple times, but it will greatly increase the computation time of the MCMC algorithm if the maximum number of delayed rejections at each iteration is too large. Delayed rejection is advantageous because it has been shown to give smaller asymptotic variances of the estimators from the chain [34]. The Adaptive Metropolis component updates the covariance of the proposal distribution based on previous iterations of the chain. This adapts the shape and size of the sampling

Table 1. Range of variation around the UNEDF1_{HFB} value for the six coupling constants included in this work. $C_t^{\rho\Delta\rho}$ and $C_t^{\rho\nabla J}$ are in MeV fm⁵ and V_0^n and V_0^p in MeV fm³.

	$C_0^{\rho\Delta\rho}$	$C_1^{\rho\Delta\rho}$	V_0^n	V_0^p	$C_0^{\rho\nabla J}$	$C_1^{\rho\nabla J}$
$\Delta\mathbf{x}$	5	50	20	15	5	25

distribution and generally makes the MCMC more efficient. In our implementation this update is only done during the burn-in phase.

4. Results

In this section, we focus on the one-dimensional potential energy curve of ²⁴⁰Pu as a function of the axial quadrupole moment, from the ground state to the point of scission. We first describe the calculations performed to generate the training data for the Gaussian process analysis. We then discuss the emulator of the potential energy curve before determining the posterior distribution of the EDF parameters.

4.1. Training runs

Gaussian processes must be trained on some input data. In our case, these consist of a set of potential energy curves for a set of N parametrizations $\mathbf{X} = (\mathbf{x}_1, \dots, \mathbf{x}_N)$ of the Skyrme functional. For each parametrization \mathbf{x}_k , we must calculate the full potential energy curve – here with triaxial deformations included. Since the parameter space of UNEDF1_{HFB} is 12-dimensional, the amount of calculation needed could quickly become gigantic. We thus imposed two restrictions to alleviate the computational cost:

- We reduced the number of varying coupling constants to 6 by keeping all bulk coupling constants fixed at their UNEDF1_{HFB} value. This is justified since these are related to nuclear matter properties and the result of the optimization shows that they are relatively well-constrained [35, 8];
- For each remaining coupling constant, we considered a rather small interval of variation centered around the nominal UNEDF1_{HFB} value, $I_t^{uu'} = [C_t^{uu'} - \Delta C_t^{uu'}, C_t^{uu'} + \Delta C_t^{uu'}]$. The quantities $\Delta C_t^{uu'}$ are listed in table 1 and correspond approximately to the standard deviations of the UNEDF1 fit; see [35].

The product set of all intervals $I_t^{uu'}$ defines a hypercube in the 6-dimensional parameter space. We sampled this hypercube with a Latin Hypercube Sampling (LHS) algorithm to determine the vector \mathbf{X} of parameterizations for the training runs. In practice, as we will show below, $N = 70$ samples were sufficient to build a high-quality emulator of the model. These included 10 runs selected using the Integrated Mean Square Prediction Error criterion (IMSPE) [36] to improve estimation of the scission point. Figure 1 shows the deformation energy (with respect to the ground-state

value) for each of the 70 samples for the case of ^{240}Pu . The end-point of each curve, usually beyond $q_{20} > 350$ b, represents the scission configuration: immediately beyond this point, the total energy drops rapidly, which manifests itself by a discontinuity in the energy curve. To increase the legibility of the figure, we did not represent this discontinuity and simply stopped the curve at scission.

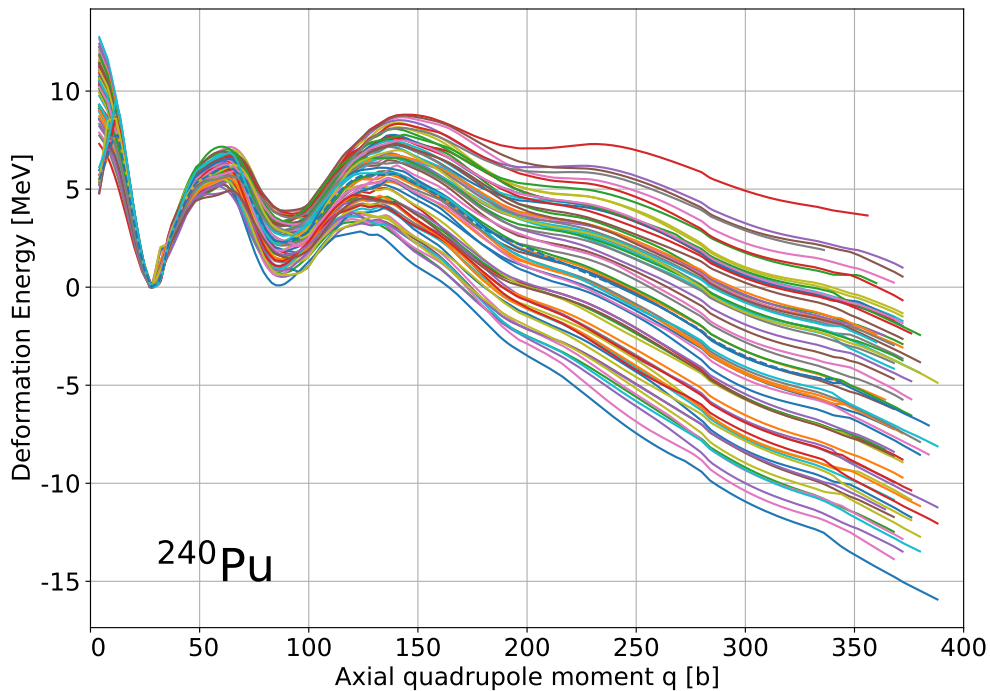


Figure 1. Deformation energy curves in ^{240}Pu as a function of the axial quadrupole moment $q \equiv \langle \hat{Q}_{20} \rangle$ for a training set of 60 different parametrizations of the Skyrme EDF. The rectangular grid guides the eye.

4.2. Emulator Fit

In this section we fit the GaSP model to the potential energy curves. For the dataset of 70 training runs, the observations were not equally spaced, but they were dense. Thus, the points used to fit the model were selected by equal spacing via interpolation. Since the scission point was not needed for calibration, the emulator was only run up to $q = 300$ b. We are not only interested in having accurate estimation of the potential energy curve for the parameter sets we have observed, but also for any parameter set within the bounds of interest. Thus, we will use cross validation to look at the out of sample error for our emulator, specifically applying leave-one-out cross validation. This is effective because it does not require additional samples, and shows what the model predictions would have been for each parameter set had the potential energy not been

observed. Figure 2 gives the leave-one-out residuals for all 70 curves. To obtain leave-one-out residuals for curve y_i , we first fit the model using the other 69 observations. Then, we use the predicted mean curve \hat{y}_i using the parameter set \mathbf{x}_i to obtain the residual.

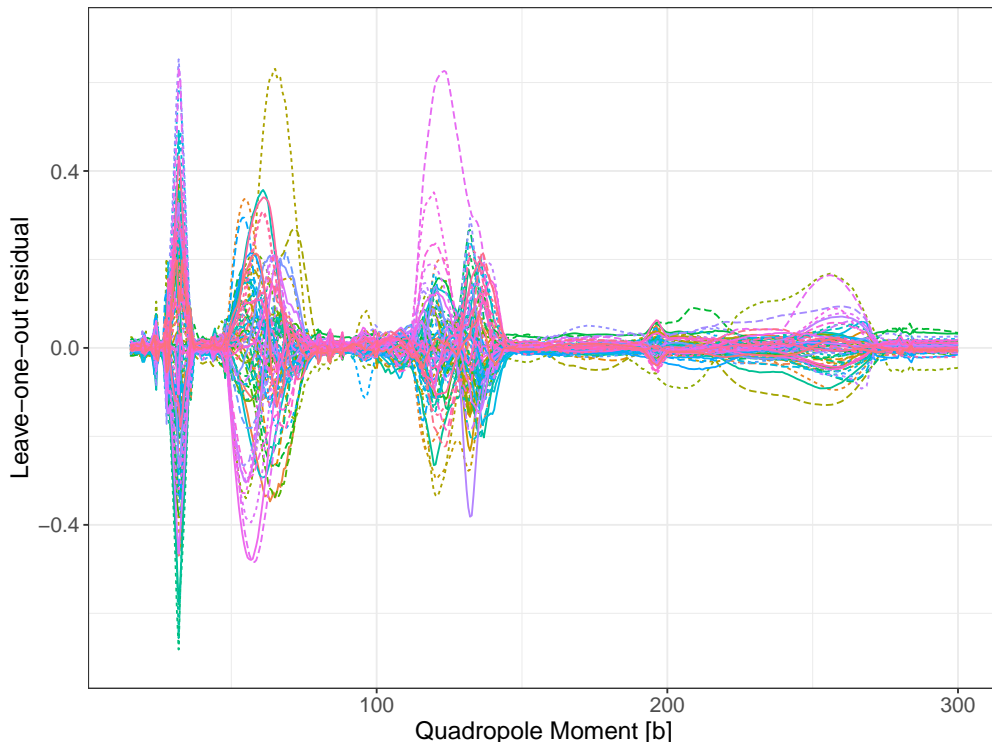


Figure 2. Leave-one-out residuals $\epsilon_{\text{GaSP}} = E(q) - E_{\text{GaSP}}(q)$ (in MeV) for the GaSP emulator as a function of the axial quadropole moment.

The results show that the largest errors ϵ_{GaSP} occur around the local maxima/minima of the potential energy curve with the areas in between having much smaller residuals. In fact, a closer analysis of the emulation error shows that it is directly connected with the onset of triaxiality. This is better visualized in figure 3, which shows the expectation values $\langle \hat{Q}_{22} \rangle$ and $\langle \hat{Q}_{30} \rangle$ as a function of the axial quadropole moment. As a reminder, the degree of triaxiality of the nuclear shape is typically characterized by the Bohr γ angle. With the conventions adopted for the multipole moments in HFODD, we have $\gamma = \text{atan}(\langle \hat{Q}_{22} \rangle / \langle \hat{Q}_{20} \rangle)$. Therefore, the shape is prolate axial if $\gamma = 0^\circ$ (hence $\langle \hat{Q}_{22} \rangle = 0$ b), oblate axial if $\gamma = 60^\circ$ ($\langle \hat{Q}_{22} \rangle = \sqrt{3} \langle \hat{Q}_{20} \rangle$), and it is maximally triaxial if $\gamma = 30^\circ$ ($\langle \hat{Q}_{22} \rangle = \sqrt{1/3} \langle \hat{Q}_{20} \rangle$).

The onset of triaxiality at $q \approx 35$ b (depending on the parameter set), the return to axial symmetry at $q \approx 60$ b, and the slightly triaxial shapes between $110 \text{ b} \leq q \leq 145$ b correspond exactly to the regions where the emulator error is maximal, reaching up to 500 keV. This is most likely the consequence of spurious discontinuities that appear in the self-consistent calculations when projecting on one-dimensional paths as in figure 2. Indeed, while the expectation value of the axial quadropole moment q is constrained,

every other moment of the nuclear surface is unconstrained. The variational principle dictates that the HFB calculation will converge to the *local* minimum nearest to the starting point. In the higher-dimensional space characterized by an additional collective variable q' , one may find at point $q = q_0$ two minima quasi-degenerate in energy but separated by a barrier along the q' direction: projecting such a surface on the q axis would give a continuous, non-differentiable curve at q_0 ; see discussion in [37]. This is exactly what seems to happen here, with $q' \equiv q_{22}$ controlling the degree of triaxiality. By contrast, the onset of octupole deformation around $q \approx 100$ b does not produce any noticeable increase in emulation error.

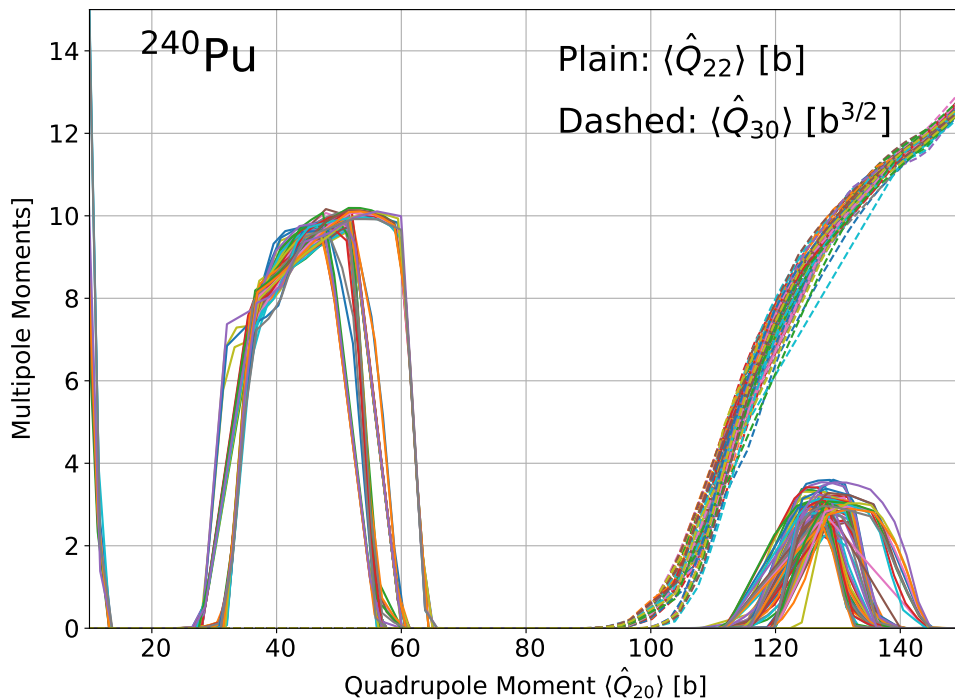


Figure 3. Expectation value $\langle \hat{Q}_{22} \rangle$ (triaxial quadrupole) and $\langle \hat{Q}_{30} \rangle$ (axial octupole) of the multipole moments as a function of the axial quadrupole moment $q \equiv \langle \hat{Q}_{20} \rangle$.

The size of this emulation error $|\epsilon_{\text{GaSP}}| \leq 0.68$ MeV should be compared to other estimates of relevant uncertainty: (i) for triaxial HFB calculations based on expansions in the one-center harmonic oscillator basis, basis truncation errors alone can easily reach a few MeV [38] (ii) while the experimental value of the fission isomer excitation energy in ^{240}Pu is known to within ± 0.2 MeV [39], this number comes from a single experiment and older estimates differ by 0.6 MeV [40] (iii) the height of both fission barriers is a model-dependent quantity extracted from fission cross sections, and the uncertainty is typically of the order of 1 MeV; see discussion in section 4.3 below.

Figure 4 shows four examples of the centered potential energy curves along with

the leave-one-out mean prediction and uncertainty from the GaSP emulator. Given the $n = 70$ samples, the centered potential energy curve $E(q, \mathbf{x}_i)$ is obtained by subtracting at each point the mean value across all samples,

$$E_{\text{cent}}(q, \mathbf{x}_i) = E(q, \mathbf{x}_i) - \frac{1}{n} \sum_{k=1}^n E(q, \mathbf{x}_k). \quad (12)$$

Centered potential energy curves with mostly negative values simply indicate that the original potential energy at each deformation q is lower than the average value at that deformation over the n samples. The four parameter sets were chosen for visual clarity and are representative of the typical performance of the emulator. From this we can see that the emulator is highly confident and also accurately captures the potential energy curves. There is more uncertainty at the minima and maxima of the curve, so the larger observed deviations from the mean prediction still largely fall within the 95% credible intervals.

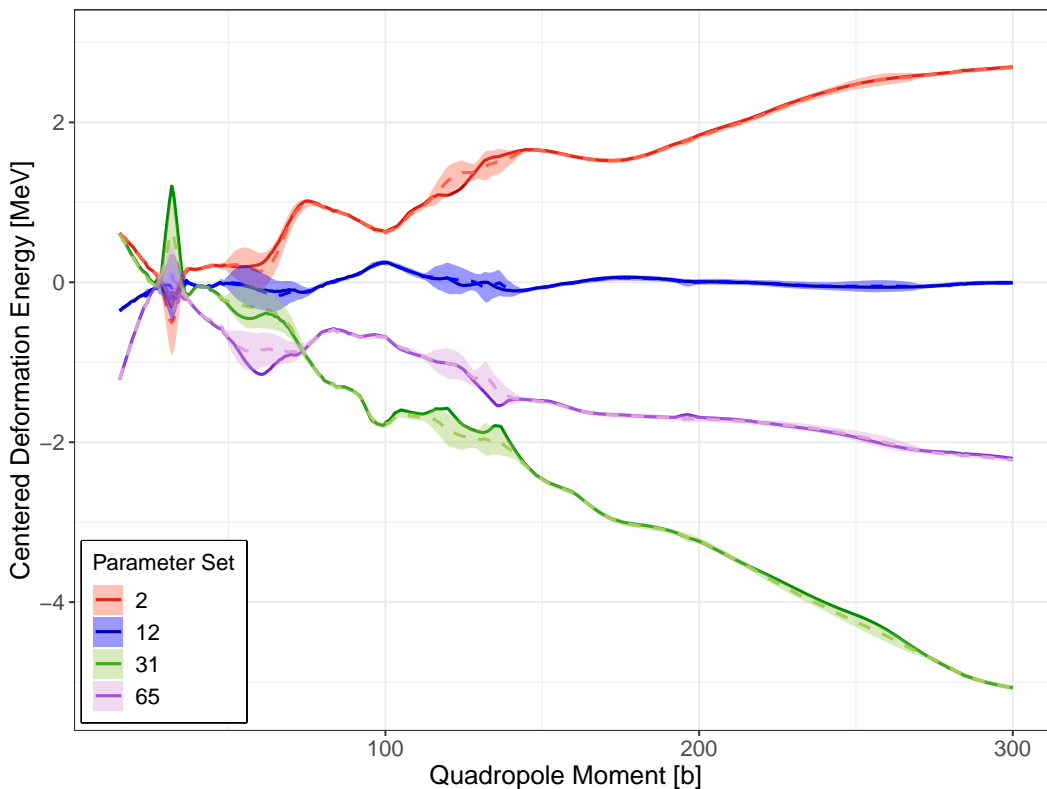


Figure 4. Centered potential energy curves with GaSP predictions. Dashed lines represent the mean prediction of the GaSP model, and shaded areas represent 95% credible intervals. The solid lines represent the simulated values.

Many relevant fission observables cannot be computed with a single collective variable q but require a higher-dimensional collective space. This is the case, for instance, with the distributions in charge, mass and kinetic energy of the fission fragments. Most importantly, these observables also need to be computed at scission, i.e., just before

the system has split into two fragments. As mentioned in the previous section, in a one-dimensional space, scission corresponds to a point (the end-point of each curve in figure 1); in a collective space of dimensions D , scission configurations correspond to a $(D - 1)$ -dimensional hypersurface. The characteristics of this surface are a function of the parameters \mathbf{x} of the functional which we need to emulate. Before embarking in such a project, which would imply running expensive calculations in a D -dimensional space, it is worth checking the ability of Gaussian processes to reproduce the scission point already in $D = 1$. In practice, we try to emulate the location q_{scis} of the discontinuity in the potential energy curve as a function of \mathbf{x} , as well as the number of particles Z_H and N_H of the heavy fragment at that point. These values are scalars and we use a simple Gaussian Process for prediction.

The leave-one-out residuals are shown in figure 5 in the form of boxplots and “violin” plots. The upper and lower portions of the box portion of the boxplot show the 25th and 75th percentile of the data, and the horizontal line in the middle shows the median. The minimum and maximum values are indicated by the ends of the vertical line going through the box; except for cases where values are far enough away from the box portion of the data (traditionally found as $1.5 \times (75\text{th percentile} - 25\text{th percentile})$ above or below the box portion). In these cases the individual points are plotted, such as the largest negative residual for the scission point. The shaded area is the violin plot and it gives an estimate of the probability distribution of the data.

Disregarding the outliers for the moment, we see that on average, the location of the scission point is reproduced within about 5 – 10 barns. The impact on the number of particles in the heavy fragment is of the order of half a particle in total. From a physics perspective, these numbers may look small, but one should bear in mind that they were obtained for the case of a one-dimensional collective space only: they are likely to increase with the size of the collective space and/or the size of the parameter space that we try to cover with the emulator even as they decrease with the number of training runs. It is not unreasonable to believe that such emulators could lead to uncertainties $\sigma_A > 1$ in the number of particles at scission. Such uncertainties have to be added to the others related to the very concept of scission; see discussion in [3]. It is also interesting to note that even though there is only one outlier for the emulation of the scission point, there are 3 of them for Z_H and A_H . This could be another manifestation of the aforementioned discontinuities, this time at scission. This effect is also likely to be further magnified when moving to higher-dimensional collective spaces. One may conclude from these results that Gaussian processes may not be the best tool to emulate the characteristics of scission.

4.3. Posterior Parameter Estimates

With the relative accuracy of the emulator established, we now proceed to obtain posterior distributions of the parameters using the GaSP emulator by conditioning on the experimental value of fission isomer excitation energy and fission barriers. This exercise

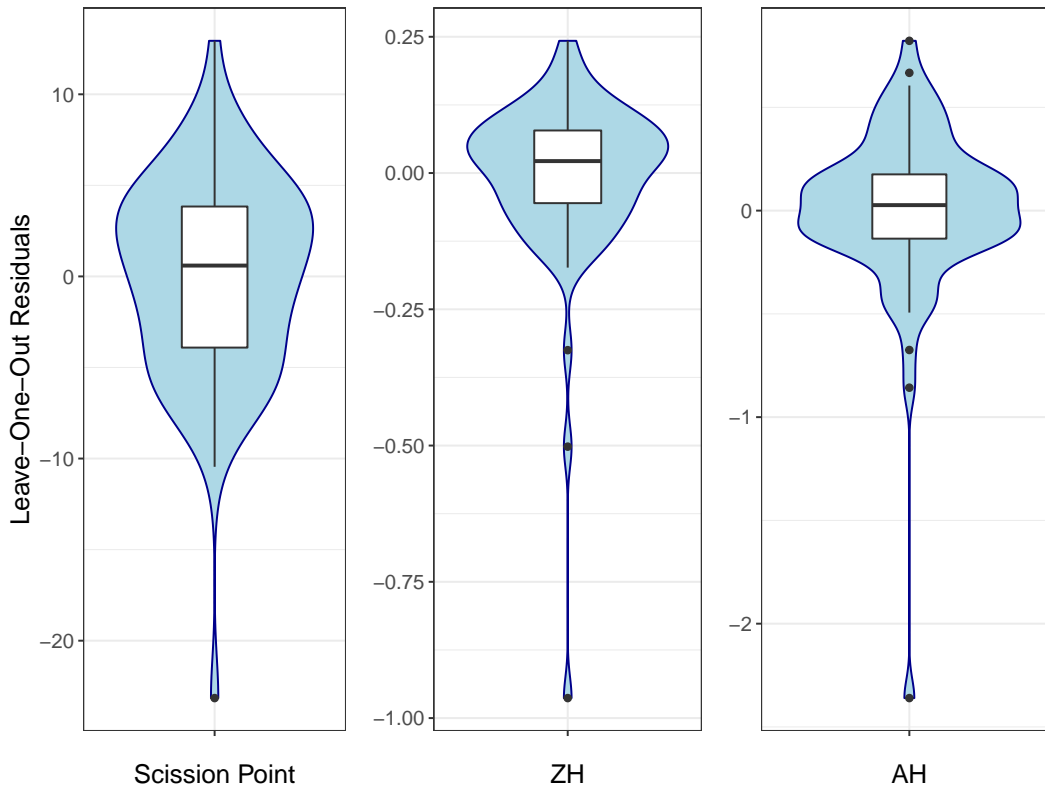


Figure 5. Boxplots overlaying violin plots for the leave-one-out prediction error for the location of the scission point, the number of protons in the heavy fragment (ZH) and the number of particles in the heavy fragment (AH)

Table 2. Summary of experimental and empirical information about the fission isomer excitation energy of ^{240}Pu and its two fission barriers. The last column is our weighted average. All units are MeV. Data for Bjornholm & Lynn is from [41]; for Capote from [42]; for Hilaire from [43]; for Hunyadi from [39] and for Singh from [40].

	Bjornholm	Capote	Hilaire	Hunyadi	Singh	Weighted
E_{FI}	2.40 ± 0.20	-	-	2.25 ± 0.20	2.80 ± 0.20	2.3500
E_{A}	5.60 ± 0.20	6.05	5.89	-	-	5.8975
E_{B}	5.10 ± 0.20	5.15	5.73	-	-	5.2825

presents two difficulties. First, there is little experimental information on the excitation energy of fission isomers and, more generally, the band-head of the lowest rotational band built on superdeformed minima [40]. Second, fission barriers are extracted from fission cross-sections in a model-dependent procedure. Typically, this analysis is based on assuming a one-dimensional, inverted parabola for the barrier [41]. As a result, fission barriers are not genuine experimental data, but empirical one, sometimes called “metadata”. Table 2 summarizes what is available in the literature for the case of ^{240}Pu .

To generate the posterior distribution we first need to define our likelihood function. When using the normal likelihood (11), posterior distributions generated about 10% of

Table 3. Values of the the six coupling constants included in this work for the original UNEDF1_{HFB} parameterization and the MAP estimate. $C_t^{\rho\Delta\rho}$ and $C_t^{\rho\nabla J}$ are in MeV fm⁵ and V_0^n and V_0^p in MeV fm³.

	$C_0^{\rho\Delta\rho}$	$C_1^{\rho\Delta\rho}$	V_0^n	V_0^p	$C_0^{\rho\nabla J}$	$C_1^{\rho\nabla J}$
UNEDF1 _{HFB}	-45.600	-143.935	-234.380	-260.437	-73.946	-51.913
MAP	-46.157	-139.972	-245.287	-250.964	-77.353	-70.143

potential energy curves with $E_A < E_B$. Since there is a relative consensus in the physics community that $E_A > E_B$, we modified the likelihood in (11) to be a truncated normal likelihood: $L(y|\mathbf{x})$ is set to be extremely small if $E_A < E_B$ so that the corresponding \mathbf{x} will not be accepted during MCMC iterations.

The values of d_i for the fission isomer excitation energy and the two fission barriers were calculated as a weighted average of the experimental or empirical values listed in table 2 based on subjective confidence estimates. Specifically, for E_{FI} , the Hunyadi value accounted for 60% of the “experimental” value while the Bjornholm and Singh numbers accounted for 30% and 10%, respectively. For both fission barriers, the Capote value accounted for 50% and the Hilaire and Bjornholm numbers for 25% each. The last column of table 2 gives the actual weighted values d_i that we used in the regression. For the calculation of the likelihood (11), the variances σ_i^2 were taken as $\sigma_i^2 = \sqrt{\sigma_{\text{exp}}^2 + \sigma_{i,\text{GaSP}}^2}$, where σ_{exp} is the experimental error, see table 4, and $\sigma_{i,\text{GaSP}}$ is the sum of the emulator standard deviation at the two locations used to calculate each excitation energy energy.

To generate the posterior samples, the first 10,000 MCMC samples were discarded in the burn-in period. The chain ran for a total of 7.5 million samples, but was thinned down to 100,000 to ensure the posterior samples were uncorrelated. The maximum a posteriori (MAP) estimator \mathbf{x}^* was found by taking the parameter set with the highest posterior probability. Table 3 compares the values of the six coupling constants for the MAP estimate and for the original UNEDF1_{HFB} parametrization. Even though the intervals of variation around the UNEDF1_{HFB} values was relatively small as shown in table 1, most parameters have changed significantly. The two-dimensional bivariate representation of the full 6-dimensional posterior distribution is shown in figure 6. Clearly, the local fit pins down the value of $C_0^{\rho\Delta\rho}$ and V_0^n , which is compatible with the analysis of [44, 45] suggesting that surface properties, which are largely dependent on the interplay between $C_0^{\rho\Delta\rho}$ and V_0^n , are highly correlated with the minima and maxima of potential energy curves. Conversely, all other coupling constants end at their boundaries, which indicates that they are not well-constrained by deformation properties.

Given the \mathbf{x}^* parameterization for the MAP estimate, we can then run the GaSP emulator for this set of coupling constants and reconstruct the entire potential energy curve. The results are shown in figure 7 together with the curve obtained from the

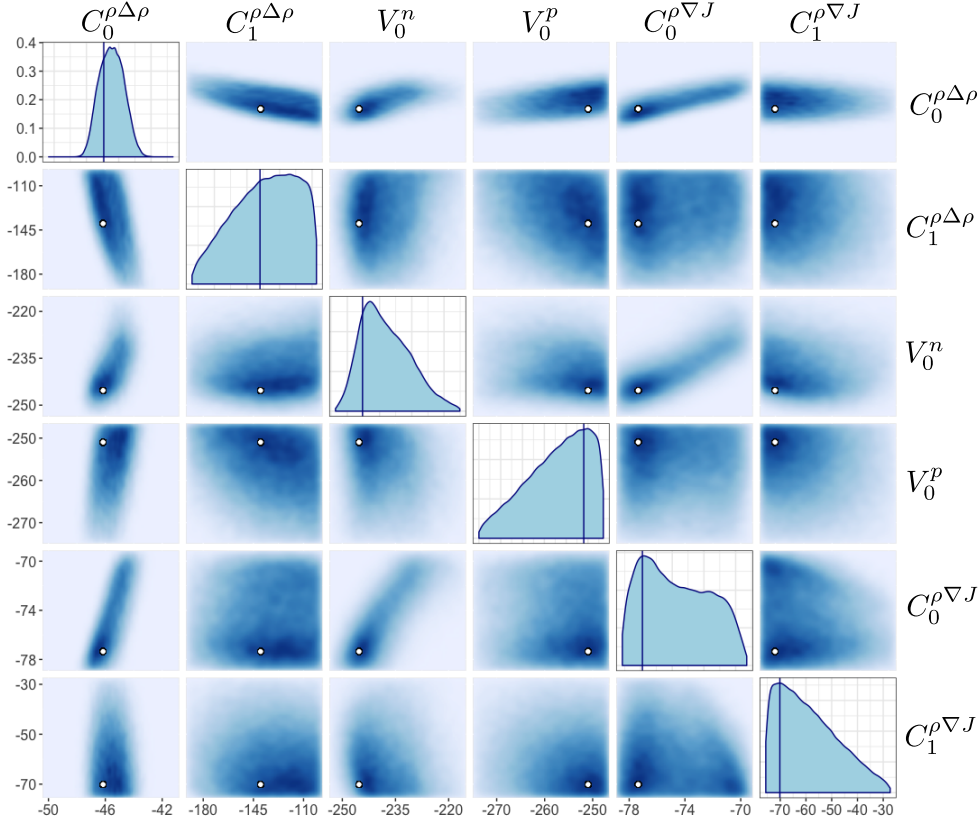


Figure 6. Posterior estimates of the parameters. The blue lines on the diagonal and the white dots with black outlines on the off diagonals indicate the MAP values.

initial UNEDF1_{HFB} parameterization. The shaded band around the MAP curve shows the 95% uncertainty from the GaSP emulator. Even if we only calibrated 3 excitation energies, E_{FI} , E_{A} and E_{B} , the Bayesian regression modifies the entire deformation energy curve. This could have a significant effect on observables such as spontaneous fission half lives τ_{SF} which are related to the quantum-mechanical tunneling probability through the barrier and thus depend both on the barrier height but also its width. Qualitatively, the τ_{SF} for ^{240}Pu computed from the MAP estimate could thus be a few orders of magnitude smaller than the value obtained with the initial parameterization of the functional, since the barriers are both lower and narrower.

The excitation energy and fission barrier heights can be extracted easily from the potential energy curves and are listed in table 4. The uncertainties are from the emulator uncertainty at the ground state and the relevant location for each energy. We recall that the empirical value used to determine the MAP solution is a weighted average of three different numbers; see table 2. In the case of the second barrier, one of the numbers is significantly different from the others, which leads to a larger uncertainty and explains why the MAP result is further away from the data.

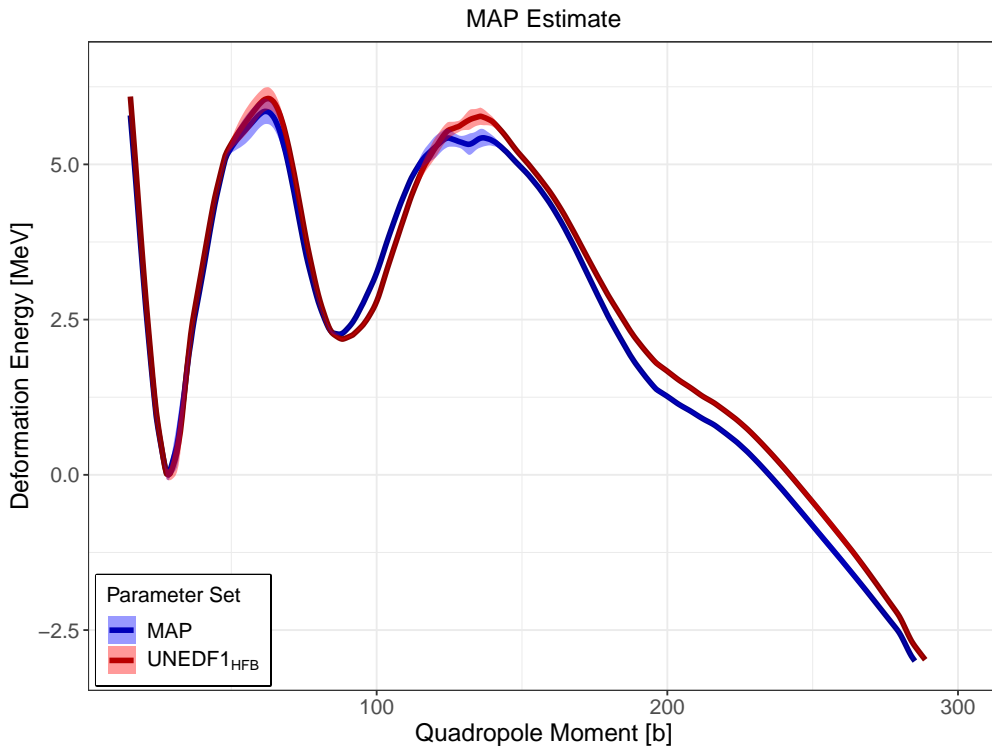


Figure 7. Potential energy curve generated using the MAP and UNEDF1_{HFB} parameterizations. In both cases, the curve was obtained from the GaSP emulator, which provides the 95% confidence region.

Table 4. Energy of the fission isomer (E_{FI}), height of the first (E_A) and second (E_B) barrier in MeV for the original UNEDF1_{HFB} functional, the parameterization that maximizes the likelihood and empirical data. We also indicate the experimental error (σ_{exp}) that was used in the regression.

	UNEDF1 _{HFB}	MAP	σ_{MAP}	Empirical	σ_{exp}
E_{FI}	2.29	2.26	0.048	2.35	0.20
E_A	6.15	5.85	0.115	5.90	0.23
E_B	5.79	5.43	0.085	5.28	0.31

5. Conclusions

In this work, we investigated the use of Gaussian processes to quantify uncertainties in nuclear deformation properties. We built an emulator of the entire one-dimensional potential energy curve in ^{240}Pu that is valid for a small 6-dimensional hypercube around the UNEDF1_{HFB} parameterization of the Skyrme functional. When the potential energy curve follows a fully-connected path in the (infinite-dimensional) collective space, the numerical precision of the emulator is excellent (less than 100 keV); when “discontinuities” occur as, e.g., triggered by the onset of triaxiality, the quality of the emulation is a little degraded but remains rather good (less than 500 keV). The location

of the scission point, which is marked as a discontinuity in the potential energy, is harder to pin-down, with uncertainties of the order of $\Delta q \approx \pm 5b$. We used our emulator to determine the posterior distribution of the coupling constants of the Skyrme energy functional conditioned on the excitation energy of the fission isomer and the height of the two fission barriers. Most of the uncertainty comes from the empirical data.

Gaussian processes belong to the class of supervised learning techniques, which themselves are part of the broader field of machine learning. In nuclear density functional theory, these techniques can be applied on at least three different classes of “data”: (1) the observable of interest, i.e., the total energy, radius, cross-section, etc. (2) matrix elements, e.g., of the mean field, pairing field or of some collective Hamiltonian and (3) the single-particle or quasiparticle wave functions. This work showed that there may be somewhat limited use in trying to emulate directly the observable of interest. The recent work of [46] suggests that working with matrix elements may hold more promise. Ultimately, one may have to directly work with individual wave functions themselves.

Acknowledgment

This work was partly performed under the auspices of the U.S. Department of Energy by Lawrence Livermore National Laboratory under Contract DE-AC52-07NA27344 and was supported by the LLNL-LDRD Program under Project No. 18-ERD-008. Computing support also came from the Lawrence Livermore National Laboratory (LLNL) Institutional Computing Grand Challenge program.

References

- [1] M. R. Mumpower, R. Surman, G. C. McLaughlin, and A. Aprahamian. The impact of individual nuclear properties on r-process nucleosynthesis. *Prog. Part. Nucl. Phys.*, 86:86, 2016.
- [2] S. A. Giuliani, Z. Matheson, W. Nazarewicz, E. Olsen, P.-G. Reinhard, J. Sadhukhan, B. Schuetrumpf, N. Schunck, and P. Schwerdtfeger. Colloquium: Superheavy elements: Oganesson and beyond. *Rev. Mod. Phys.*, 91(1):011001, 2019.
- [3] N Schunck and L M Robledo. Microscopic theory of nuclear fission: A review. *Rep. Prog. Phys.*, 79(11):116301, 2016.
- [4] R.M. Dreizler and E.K.U Gross. *Density Functional Theory: An Approach to the Quantum Many-Body Problem*. Springer-Verlag, 1990.
- [5] R. Eschrig. *Fundamentals of Density Functional Theory*. Teubner, Leipzig, 1996.
- [6] Nicolas Schunck. *Energy Density Functional Methods for Atomic Nuclei*. IOP Expanding Physics. IOP Publishing, Bristol, UK, 2019. OCLC: 1034572493.
- [7] N. Schunck, J. D. McDonnell, D. Higdon, J. Sarich, and S. Wild. Quantification of Uncertainties in Nuclear Density Functional Theory. *Nucl. Data Sheets*, 123:115, 2015.
- [8] Nicolas Schunck, Jordan D. McDonnell, Jason Sarich, Stefan M. Wild, and Dave Higdon. Error analysis in nuclear density functional theory. *J. Phys. G: Nucl. Part. Phys.*, 42(3):034024, 2015.
- [9] N. Schunck, J. D. McDonnell, D. Higdon, J. Sarich, and S. M. Wild. Uncertainty Quantification and Propagation in Nuclear Density Functional Theory. *Eur. Phys. J. A*, 51(12):1, 2015.
- [10] Y. Gao, J. Dobaczewski, M. Kortelainen, J. Toivanen, and D. Tarpanov. Propagation of uncertainties in the Skyrme energy-density-functional model. *Phys. Rev. C*, 87(3):034324, 2013.

- [11] S. Goriely and R. Capote. Uncertainties of mass extrapolations in Hartree-Fock-Bogoliubov mass models. *Phys. Rev. C*, 89(5):054318, 2014.
- [12] R. Utama, J. Piekarewicz, and H. B. Prosper. Nuclear mass predictions for the crustal composition of neutron stars: A Bayesian neural network approach. *Phys. Rev. C*, 93(1):014311, 2016.
- [13] T. Haverinen and M. Kortelainen. Uncertainty propagation within the UNEDF models. *J. Phys. G: Nucl. Part. Phys.*, 44(4):044008, 2017.
- [14] Léo Neufcourt, Yuchen Cao, Witold Nazarewicz, and Frederi Viens. Bayesian approach to model-based extrapolation of nuclear observables. *Phys. Rev. C*, 98(3):034318, 2018.
- [15] Léo Neufcourt, Yuchen Cao, Witold Nazarewicz, Erik Olsen, and Frederi Viens. Neutron Drip Line in the Ca Region from Bayesian Model Averaging. *Phys. Rev. Lett.*, 122(6):062502, 2019.
- [16] M. Kortelainen, J. Erler, W. Nazarewicz, N. Birge, Y. Gao, and E. Olsen. Neutron-skin uncertainties of Skyrme energy density functionals. *Phys. Rev. C*, 88(3):031305, 2013.
- [17] P.-G. Reinhard and W. Nazarewicz. Information content of the low-energy electric dipole strength: Correlation analysis. *Phys. Rev. C*, 87(1):014324, 2013.
- [18] N. Paar, Ch. C. Moustakidis, T. Marketin, D. Vretenar, and G. A. Lalazissis. Neutron star structure and collective excitations of finite nuclei. *Phys. Rev. C*, 90(1):011304, 2014.
- [19] J. D. McDonnell, N. Schunck, D. Higdon, J. Sarich, S. M. Wild, and W. Nazarewicz. Uncertainty Quantification for Nuclear Density Functional Theory and Information Content of New Measurements. *Phys. Rev. Lett.*, 114(12):122501, 2015.
- [20] J.-P. Blaizot and G. Ripka. *Quantum Theory of Finite Systems*. The MIT Press, Cambridge, 1985.
- [21] P. Ring and P. Schuck. *The Nuclear Many-Body Problem*. Texts and Monographs in Physics. Springer, 2004.
- [22] Y. M. Engel, D. M. Brink, K. Goeke, S. J. Krieger, and D. Vautherin. Time-dependent Hartree-Fock theory with Skyrme’s interaction. *Nucl. Phys. A*, 249(2):215, 1975.
- [23] J. Dobaczewski and J. Dudek. Time-Odd Components in the Rotating Mean Field and Identical Bands. *Acta Phys. Pol. B*, 27(1):45, 1996.
- [24] Michael Bender, Paul-Henri Heenen, and Paul-Gerhard Reinhard. Self-consistent mean-field models for nuclear structure. *Rev. Mod. Phys.*, 75(1):121, 2003.
- [25] E. Perlińska, S. G. Rohoziński, J. Dobaczewski, and W. Nazarewicz. Local density approximation for proton-neutron pairing correlations: Formalism. *Phys. Rev. C*, 69(1):014316, 2004.
- [26] T. Lesinski, M. Bender, K. Bennaceur, T. Duguet, and J. Meyer. Tensor part of the Skyrme energy density functional: Spherical nuclei. *Phys. Rev. C*, 76(1):014312, 2007.
- [27] M. Kortelainen, T. Lesinski, J. Moré, W. Nazarewicz, J. Sarich, N. Schunck, M. V. Stoitsov, and S. Wild. Nuclear energy density optimization. *Phys. Rev. C*, 82(2):024313, 2010.
- [28] E. Chabanat, P. Bonche, P. Haensel, J. Meyer, and R. Schaeffer. A Skyrme parametrization from subnuclear to neutron star densities Part II. Nuclei far from stabilities. *Nucl. Phys. A*, 635(1):231, 1998.
- [29] N. Schunck, J. Dobaczewski, W. Satuła, P. Bączyk, J. Dudek, Y. Gao, M. Konieczka, K. Sato, Y. Shi, X. B. Wang, and T. R. Werner. Solution of the Skyrme-Hartree-Fock-Bogolyubov equations in the Cartesian deformed harmonic-oscillator basis. (VIII) HFODD (v2.73y): A new version of the program. *Comput. Phys. Commun.*, 216:145, 2017.
- [30] N. Schunck, D. Duke, H. Carr, and A. Knoll. Description of induced nuclear fission with Skyrme energy functionals: Static potential energy surfaces and fission fragment properties. *Phys. Rev. C*, 90(5):054305, 2014.
- [31] Mengyang Gu, Xiaojing Wang, James O Berger, et al. Robust gaussian stochastic process emulation. *The Annals of Statistics*, 46(6A):3038–3066, 2018.
- [32] Mengyang Gu, Jesus Palomo, and James Berger. *RobustGaSP: Robust Gaussian Stochastic Process Emulation*, 2019. R package version 0.5.7.
- [33] Heikki Haario, Marko Laine, Antonietta Mira, and Eero Saksman. Dram: efficient adaptive mcmc. *Statistics and computing*, 16(4):339–354, 2006.

- [34] Luke Tierney and Antonietta Mira. Some adaptive monte carlo methods for bayesian inference. *Statistics in medicine*, 18(17-18):2507–2515, 1999.
- [35] M. Kortelainen, J. McDonnell, W. Nazarewicz, P.-G. Reinhard, J. Sarich, N. Schunck, M. V. Stoitsov, and S. M. Wild. Nuclear energy density optimization: Large deformations. *Phys. Rev. C*, 85(2):024304, 2012.
- [36] Thomas J Santner, Brian J Williams, William Notz, and Brian J Williams. *The design and analysis of computer experiments*, volume 1. Springer, 2003.
- [37] N. Dubray and D. Regnier. Numerical search of discontinuities in self-consistent potential energy surfaces. *Comput. Phys. Commun.*, 183(10):2035, 2012.
- [38] N. Schunck. Density Functional Theory Approach to Nuclear Fission. *Acta Phys. Pol. B*, 44:263, 2013.
- [39] M. Hunyadi, D. Gassmann, A. Krasznahorkay, D. Habs, P. G. Thirolf, M. Csatlós, Y. Eisermann, T. Faestermann, G. Graw, J. Gulyás, R. Hertenberger, H. J. Maier, Z. Máté, A. Metz, and M. J. Chromik. Excited superdeformed $K^\pi=0+$ rotational bands in β -vibrational fission resonances of ^{240}Pu . *Phys. Lett. B*, 505(1):27–35, 2001.
- [40] Balraj Singh, Roy Zywina, and Richard B. Firestone. Table of superdeformed nuclear bands and fission isomers: (october 2002). *Nucl. Data Sheets*, 97(2):241, 2002.
- [41] S. Bjørnholm and J. E. Lynn. The double-humped fission barrier. *Rev. Mod. Phys.*, 52(4):725, 1980.
- [42] R. Capote, M. Herman, P. Obložinský, P.G. Young, S. Goriely, T. Belgia, A.V. Ignatyuk, A.J. Koning, S. Hilaire, V.A. Plujko, M. Avrigeanu, O. Bersillon, M.B. Chadwick, T. Fukahori, Zhigang Ge, Yinlu Han, S. Kailas, J. Kopecky, V.M. Maslov, G. Reffo, M. Sin, E.Sh. Soukhovitskii, and P. Talou. RIPL – Reference Input Parameter Library for Calculation of Nuclear Reactions and Nuclear Data Evaluations. *Nucl. Data Sheets*, 110(12):3107, 2009.
- [43] S. Goriely, S. Hilaire, A. J. Koning, M. Sin, and R. Capote. Towards a prediction of fission cross sections on the basis of microscopic nuclear inputs. *Phys. Rev. C*, 79(2):024612, 2009.
- [44] N. Nikolov, N. Schunck, W. Nazarewicz, M. Bender, and J. Pei. Surface symmetry energy of nuclear energy density functionals. *Phys. Rev. C*, 83(3):034305, 2011.
- [45] W. Ryssens, M. Bender, K. Bennaceur, P.-H. Heenen, and J. Meyer. Impact of the surface energy coefficient on the deformation properties of atomic nuclei as predicted by Skyrme energy density functionals. *Phys. Rev. C*, 99(4):044315, 2019.
- [46] Raphaël-David Lasserri, David Regnier, Jean-Paul Ebran, and Antonin Penon. Taming Nuclear Complexity with a Committee of Multilayer Neural Networks. *Phys. Rev. Lett.*, 124(16):162502, 2020.